Far-infrared to millimeter astrophysical dust emission

II: Comparison of the two-level systems (TLS) model with astronomical data

D. Paradis[1,2], J.-Ph. Bernard[1,2], C. Mény[1,2], and V. Gromov[1,2,3]

[1] Université de Toulouse; UPS-OMP; IRAP; Toulouse, France
[2] CNRS; IRAP; 9 Av. du Colonel Roche, BP 44346, F-31028 Toulouse cedex 4, France
[3] Space Research Institute, RAS, 84/32 Profsoyuznaya, 117810 Moscow, Russia

ABSTRACT

Aims. In a previous paper we proposed a new model for the emission by amorphous astronomical dust grains, based on solid-state physics. The model uses a description of the disordered charge distribution (DCD) combined with the presence of two-level systems (TLS) defects in the amorphous solid composing the grains. The goal of this paper is to compare this new model to astronomical observations of different Galactic environments in the far-infrared/submillimeter, in order to derive a set of canonical model parameters to be used as a Galactic reference to be compared to in future Galactic and extragalactic studies.

Methods. We compare the TLS model with existing astronomical data. We consider the average emission spectrum at high latitudes in our Galaxy as measured with FIRAS and WMAP, as well as the emission from Galactic compact sources observed with the Archeops balloon experiment, for which an inverse relationship between the dust temperature and the emissivity spectral index (β) has been proven.

Results. We show that, unlike models previously proposed that often invoke two dust components at different temperatures, the TLS model successfully reproduces both the shape of the Galactic spectral energy distribution and its evolution with temperature as observed in the Archeops data. The best TLS model parameters indicate a charge coherence length of $\simeq 13$ nm and other model parameters in broad agreement with expectations from laboratory studies of dust analogs. We conclude that the millimeter excess emission, which is often attributed to the presence of very cold dust in the diffuse ISM, is very likely caused solely by TLS emission in disordered amorphous dust grains. We discuss the implications of the new model, in terms of mass determinations from millimeter continuum observations and the expected variations in the emissivity spectral index with wavelength and dust temperature. The implications for analyzing of the Herschel and Planck satellite data are discussed.

1. Introduction

Early astronomical observations in the far-infrared (FIR) and submillimeter (submm) range have revealed the spectral energy distribution (SED) of dust emission towards the diffuse interstellar medium (ISM) to be consistent with a modified black-body function of the form

$$I_\nu(\lambda) = \epsilon_e \, B_\nu(\lambda, T_d) \times N_H \tag{1}$$

where I_ν is the specific intensity or sky brightness (energy flux per unit wavelength and solid angle), B_ν the Planck function, λ the wavelength, T_d the dust equilibrium temperature, and N_H the hydrogen column density. Those measurements were found to be consistent with a power-law emissivity function:

$$\epsilon_e = \epsilon(\lambda_0) \left(\frac{\lambda}{\lambda_0} \right)^{-\beta} \tag{2}$$

where $\epsilon(\lambda_0)$ is the emissivity at the reference wavelength λ_0, and β is the emissivity spectral index, usually taken as $\beta = 2$ (the so-called quadratic law). The quality of the available data generally did not allow checking for variations in β, which was therefore assumed to be constant.

The emission originates in dust radiating at thermal equilibrium (at the temperature T_d) with the surrounding radiation

field, and as a consequence is related to the FIR and submm optical properties of the dust. Considering a constant gas/dust ratio N_H/M_d (with M_d the mass column density), and assuming a single dust temperature along the line of sight (LOS), the specific intensity can be written as

$$I_\nu(\lambda) = \kappa(\lambda_0) \left(\frac{\lambda}{\lambda_0} \right)^{-\beta} B_\nu(\lambda, T_d) \times M_d, \tag{3}$$

with

$$\kappa(\lambda_0) = \epsilon(\lambda_0) \frac{N_H}{M_d} \tag{4}$$

where $\kappa(\lambda_0)$ is the dust mass opacity at the reference wavelength λ_0.

In solid state physics, within the framework of classical models, a constant and temperature-independent emissivity spectral index value $\beta = 2$ is justified by the asymptotic behavior of the absorption cross-section of solids at long wavelengths, far from the absorption resonances, such as the silicate absorption features at 10-20 μm. However, it was recognized early that the quadratic law may not hold for amorphous materials in the FIR/submm, since such materials are likely to exhibit low-energy transitions that happen in the FIR/submm (see Andriesse, 1974). Although big grains (BGs) are known to be amorphous in nature in the diffuse ISM (Kemper et al., 2004), no need was identified to explicitly incorporate details about their internal structure in astrophysical models due to the lack of submm

data. However, recent observations have proven that the actual FIR/submm dust SED is significantly more complicated than described by Eq. 2.

Several recent studies have shown evidence of variations in the dust emissivity law with wavelength. That the overall Galactic SED is flatter than predicted by the quadratic law was clearly shown in the FIRAS data by Reach et al. (1995). Paradis et al. (2009) studied the spectral dependence of dust emission in a collection of molecular clouds and their atomic surroundings over the spectral range covered by the DIRBE, Archeops, and WMAP experiments and showed that the observed emissivity law exhibits a break around 500 μm, with a steeper index (β=2.4) in the FIR and a flatter index (β=1.5) in the submm. More recently a similar trend has been apparent in the Planck data of the Taurus molecular cloud (Planck collaboration, 2011g). Similar submm excess emission has also been observed towards external low-metallicity galaxies Galliano et al. (2005), as well as towards the Small Magellanic Cloud in the Planck data (Planck collaboration, 2011a). The comparison between the spectral indices derived for the Galactic solar neighborhood ($\beta = 1.8$), the LMC ($\beta = 1.5$), and the SMC ($\beta = 1.2$) in the Planck data by Planck collaboration (2011b,a) indicates a general flattening that could be linked to the varying metallicity among these three environments. It therefore appears that the dust SED is usually flatter than predicted by the quadratic law and that the associated emissivity index β varies with wavelength and from object to object, possibly tracing evolution of the dust properties with metallicity.

In addition to the above, the spectral index of the dust emission as derived from a modified black-body fit to the data follows a systematic trend with dust temperature, the emissivity spectrum appearing flatter for regions with warmer dust temperatures and steeper for colder regions.

- Dupac et al. (2003) show variations in β in the FIR in various regions of the ISM, using the PRONAOS balloon-borne experiment data. They found variations in the index in the range 2.4 to 0.8 for T_d between 11 and 80 K.
- Désert et al. (2008) highlighted variations in β in the submm towards compact sources in Archeops balloon-borne experiment data. They found variations in the index in the range 4 to 1 for temperatures between 7 and 27 K.
- Veneziani et al. (2010) show variations in β between 5 and 1 in the temperature range 7-20 K by analyzing 8 high Galactic latitudes clouds using BOOMERanG observations, combined with the IRAS, DIRBE, and WMAP data.
- Paradis et al. (2010) found evidence of T_d-β variations using the combination of the new Herschel and IRAS data, in the inner regions of the Galactic plane. The β range is 2.6-1.8 for temperatures between 14 and 23 K.

The origin of the flatness of the dust emission spectrum observed with FIRAS has been explored by Reach et al. (1995) and Finkbeiner et al. (1999). The latter group propose a phenomenological description of the FIRAS data that invokes the coexistence of a warm ($T_d \simeq 16\,K$) and a very cold dust ($T_d \simeq 9\,K$) component (hereafter FDS model). Reach et al. (1995) determined that the FIR and the submm emission were tightly correlated and therefore did not favor the very cold dust component.

Moreover, the two component description does not reproduce the observed variations in the emissivity spectral index with dust temperature. Indeed the spectral index associated to each of the components is set to a fixed value in the FDS model. For instance, in their best-fit model, β for the cold silicate-like component is set to 1.7, which does not allow SEDs to be produced

with a larger apparent emissivity index in the submm/mm domain (see Section 5.1).

The two-level systems (TLS) model (Mény et al., 2007, hereafter Paper I) has been developed to describe the FIR to mm continuum interstellar dust emission, taking the effect of the disordered internal structure of the amorphous dust grains into account. It is based on the solid-state physics model developed to interpret specific properties of the amorphous solids identified in laboratory data. As a consequence, it is expected to apply with a high degree of universality, and not to be sensitive to the exact chemical nature of the dust. The disordered charge distribution (DCD) part of the model describes the interaction between the electromagnetic wave and acoustic oscillations in the disordered charge of the amorphous material (Vinogradov, 1960; Schlömann, 1964). This charge-disorder is observed on nanometer scale and is described here by a single charge correlation length. The TLS part of the model describes the interaction of the electromagnetic wave with a simple distribution of asymmetric double-well potential (ADWP), which results from disorder on atomic scale: a ADWP can be associated with two close configurations of atoms or group of atoms in the disordered structure (Phillips, 1972, 1987; Anderson et al., 1972), where the corresponding atoms have two equilibrium positions and can transit from one to the other. Both DCD and TLS phenomena have been first applied by Bösch (1978) to explain the observed temperature dependence of the absorption of some silica-based glasses in the FIR/mm.

In section 2, we present the data we consider for this analysis. In section 3, we briefly describe the model in terms of the disordered structure, as well as the main parameters of the model. In section 4, we explain the methods we used to compare the model to astrophysical data and derive standard parameters for the Milky Way (MW). In section 5, we present model predictions for the standard parameters derived above, such as the evolution of the dust emission with temperature, the emissivity spectral index as a function of wavelength and temperature, and the predicted emissivity in Herschel and Planck photometric bands. Sections 6 and 7 are devoted to the discussion and conclusions, respectively.

2. Astronomical data

In the following we describe the dataset we used in this study.

2.1. FIR/mm SED of the diffuse Milky Way emission

The shape of the dust SED in the diffuse medium is an important constraint on the physics of interstellar dust. In principle, we would like to compare the new model with the SED of the most nearby and the most diffuse ISM, in order to avoid including emission from dense regions where dust properties may differ from those in the diffuse solar neighborhood. Also, it is important to analyze regions with minimum temperature mixing along the LOS, which may make the interpretations difficult. However, waiting for the Planck data to become publicly available, the data presently available prevent us from deriving such an SED up to millimeter wavelengths, because the low dust emissivity in this range and the low dust column density available combine into a poor signal to noise ratio (S/N). For instance, the solar neighborhood SED presented by Boulanger et al. (1996) did not allow measuring dust emission in the solar neighborhood for $\lambda > 1.1$ mm. Instead, we used the emission from the whole MW, but exclude the central parts of the Galactic disk ($|b| < 6°$) in order to avoid regions with extensive dust property mixing along the

LOS, as well as regions with $I_{240} < 18$ MJy/sr, to keep a reasonable S/N. Figure 1 shows the region of the sky seen by FIRAS at 240 μm that we considered in this work, which accounts for 13.7% of the entire sky.

We constructed an average MW SED from 100 μm to 13 mm (23 GHz) by merging data from the FIRAS instrument onboard the COBE satellite and the WMAP data. We used the full range of FIRAS wavelengths (0.1-10 mm or 3000-30 GHz) and the 5 WMAP bands at 13 mm (23 GHz), 9.1 mm (33 GHz), 7.3 mm (41 GHz), 4.9 mm (61 GHz) and 3.2 mm (94 GHz). The angular resolution of the FIRAS data is assumed to be 7°. The angular resolution of the WMAP data is taken from the WMAP explanatory supplement to range from 13′ to 53′ with increasing wavelengths.

For practical purposes, the FIRAS data were first reprojected into the all-sky pixelisation scheme HEALPix (Hierarchical Equal Area isoLatitude Pixelization) so that it can easily be combined with the WMAP data. This was done using the method currently used for all Planck ancillary data and described in Paradis et al. (2011). The FIRAS data used here are available in the HEALPix scheme on the WMAP LAMBDA (Legacy Archive for Microwave Background Data) website[1]. The WMAP data were degraded to the FIRAS angular resolution (7°) through the convolution with a Gaussian kernel of the appropriate FWHM using the standard convolution tools in HEALPix, before extracting the SED. An offset subtraction was done by removing an average SED computed over regions of the sky with low emission set as $I_{240} < 3$ MJy/sr, corresponding to high Galactic latitudes. The method used removes any arbitrary additive offset in the data that could be set by calibration uncertainty or cosmological sources such as the cosmic infrared background (CIB). Uncertainties on the SED are computed as the quadratic sum of three different uncertainties for each instrument: calibration, white noise per pixel, and background. We assumed the official calibration and white noise uncertainties given in the explanatory supplements. Calibration uncertainties are ≤10% for FIRAS, depending on the frequency range, and less than 1% for WMAP data (Jarosik et al., 2011). The background uncertainties on the FIRAS and WMAP data have been derived by computing the standard deviation over fifty circular regions with a 2° radius, taken randomly in the high latitude sky. This uncertainty largely predominates over the other ones.

The obtained SED is shown in Figure 2, and the SED values and uncertainties are given in Table 1. The corresponding average HI column density is 2×10^{21} H/cm². It can be seen from Figure 2 that the emission peaks near $\lambda = 160 \mu$m, in agreement with the FIRAS SED derived at high latitudes by Boulanger et al. (1996), who found an average dust temperature of 17.5 K assuming a constant spectral index set to 2. The recent analysis of the Planck data shows that a more appropriate value for the FIR spectral index in the solar neighborhood is $\beta = 1.8$ (Planck collaboration, 2011a), and using this value over nine fields in the galactic halo leads to a similar temperature value of 17.9 K (Planck collaboration, 2011f) and 17.7 K for regions with $|b| > 10°$. Above $\lambda \simeq 5$ mm, the ISM emission starts increasing with wavelengths. This contribution does not originate in thermal dust emission, but is most probably from a combination of synchrotron or free-free emission and/or to anomalous microwave emission, which is often attributed to spinning dust (see for instance Finkbeiner et al., 2004; Planck collaboration, 2011c,d)

---

[1] http://lambda.gsfc.nasa.gov/

2.2. FIR/submm SEDs of Galactic compact sources

Before the Planck data become publicly available, the FIRAS data are the only data allowing the dust equilibrium temperature and the FIR-submm spectral index of dust emission to be measures simultaneously over large regions of the sky. This is mainly because this requires both FIR data (which measure temperature best) and submm data in the Rayleigh-Jeans regime, which constrains the submm emissivity index best. The FIRAS data accurately sample the peak of the BG emission. A good sampling of data in the range 100- 500 μm is crucial for constraining the dust temperature, as well as the correlation length, which is a free parameter of the TLS model (see Section 3.2). Unfortunately, at the angular resolution of the FIRAS instrument, the sky distribution provides very little handle on dust temperature variations. At the FIRAS resolution, the dust temperature varies only from 16 to 21 K (Reach et al., 1995), assuming a constant spectral index equal to 2. Therefore, testing the temperature dependence of the dust spectral index requires additional information in the submm over wide dust temperature range.

Balloon experiments have been able to record FIR/submm data at a significantly better angular resolution than for the COBE and FIRAS data. Both the PRONAOS and the Archeops data analysis (Dupac et al., 2001; Désert et al., 2008) show a decrease in the spectral index with temperature. The former study used data of the diffuse emission mapped over limited regions going from cirrus clouds to dense regions. The latter study was carried using observations of compact sources in the MW. The variations sample the range from $\beta \simeq 4$ for compact sources with dust temperatures as low as 7 K down to $\beta \simeq 1$ for the highest temperatures of about 27 K. The interpretation of the observed variations in the emissivity index with temperature is still being debated. Shetty et al. (2009) argue that the observed anti-correlation could result entirely from noise in the data or from temperature mixing along the LOS. However, the recent analysis of the Herschel data in the Galactic plane by Paradis et al. (2010) demonstrated that the observed variations could not be entirely due to data noise. Similarly, the analysis of the Planck data towards cold cores showed that the expected LOS temperature mixing could not explain the whole observed trend. It is therefore likely that the observed steepening of the emissivity index with decreasing temperature reveals changes in the optical properties of astronomical dust with temperature. Laboratory experiments (Boudet et al., 2005; Coupeaud et al., 2011) have also shown evidence of a similar behavior for analogs of the amorphous material likely to compose astrophysical dust grains, which tend to favor actual variations in the dust properties with temperature.

Here, we do not intend to fit any given T_d-β relationship. Instead, we minimize against the overall Archeops compact source spectra, which do not impose following a predetermined T_d-β relationship. Archeops observed about 30% of the sky at a 12′ angular resolution, in four photometric bands: 550, 850, 1382 and 2098 μm (Benoît et al., 2003). The Archeops compact sources catalog (Désert et al., 2008) contains 302 SEDs, which have been fitted using a modified black body. Only 153 fits have given a satisfactory χ^2 (using a χ^2 goodness-of-fit criteria at the 2-σ level) when using free T_d and β (Désert et al., 2008). We therefore restricted our analysis to these 153 spectra. Since the sampling of the compact sources spectra is not evenly distributed in dust temperatures, we averaged them in ten bins of temperature, between 7.3 and 25.7 K. In this way, we ensure a similar weight for the ten spectra. The summary of the binning parameters, including the bin's central temperature, the average fluxes,

λ (μm)	104.0	106.5	109.2	111.9	114.9	117.9	121.2	124.6	128.2	132.1	136.1	140.5	145.1
Brightness (MJy/sr)	17.08	24.79	26.28	30.92	30.73	33.27	32.93	34.55	35.72	36.40	37.87	38.86	39.34
1-σ (MJy/sr)	49.38	15.95	11.24	11.66	7.22	7.66	6.48	6.49	4.58	4.37	3.13	2.75	2.28
λ (μm)	150.0	155.3	161.0	167.1	173.6	180.8	188.5	196.9	206.1	216.2	227.3	239.7	253.5
Brightness (MJy/sr)	40.15	39.90	41.82	40.76	40.86	40.29	39.33	38.13	36.66	34.68	32.51	30.18	27.57
1-σ (MJy/sr)	2.75	2.20	1.39	1.29	0.99	1.50	1.16	0.91	0.53	0.44	0.35	0.28	0.29
λ (μm)	268.9	286.4	306.3	329.1	355.7	386.9	424.1	469.2	525.1	596.0	698.1	816.9	1002.4
Brightness (MJy/sr)	24.92	22.12	19.35	16.62	14.01	11.53	9.37	7.22	5.21	3.66	2.46	1.49	0.79
1-σ (MJy/sr)	0.25	0.35	0.22	0.24	0.24	0.24	0.29	1.01	0.33	0.17	0.12	0.11	0.09

λ (μm)	1297.2	1837.7	3150.3	3200.0	4900.0	7300.0	9100.0	13000.0
Brightness (MJy/sr)	0.35	0.13	-1.6×10^{-2}	1.9×10^{-2}	9.2×10^{-3}	9.8×10^{-3}	1.1×10^{-2}	1.5×10^{-2}
1-σ (MJy/sr)	0.10	0.10	0.12	1.1×10^{-3}	5.6×10^{-4}	2.7×10^{-4}	2.3×10^{-4}	1.8×10^{-4}

Table 1. FIRAS/WMAP SED of the diffuse MW emission.

the number of sources, as well as their Archeops names, are provided in Table 2.

The uncertainty on the data is the quadratic combination of the relative and the absolute uncertainties (15, 17, 21, and 14 % from 550 μm to 2.1 mm).

3. The TLS model

In the following, we first remind the reader of the relation between dust emission and absorption and then briefly summarize the different processes of the TLS model. The full theoretical description of the model is given in Paper I.

3.1. Relation between dust emission and absorption

The Mie theory is based on the exact resolution of the Maxwell's equation for the absorption and scattering of a plane electromagnetic wave by a homogeneous spherical particle whose material is characterized by its complex dielectric constant $\epsilon(\omega) = \epsilon'(\omega) + i\epsilon''(\omega)$, with $\omega = 2\pi c/\lambda$. Solid state physical models often analyze the optical properties by the use of the complex susceptibility $\chi_0(\omega) = \chi'(\omega) + i\chi''(\omega)$, which in the case of isotropic dielectric materials is related to the complex dielectric constant by the Clausius-Mossotti equation:

$$\epsilon(\omega) = 1 + \frac{4\pi\chi_0(\omega)}{1 - \frac{4\pi\chi_0(\omega)}{3}}. \tag{5}$$

For spherical grains of radius a and density ρ, the Mie theory gives the following expression for the dust mass opacity:

$$\kappa(\omega) = \frac{9\omega}{\rho c} Im\left(\frac{\epsilon(\omega) - 1}{\epsilon(\omega) + 2}\right). \tag{6}$$

The optical properties of bulk materials are also often characterized by the absorption coefficient α, which is defined as the optical depth τ in the bulk material per unit length. The absorption coefficient α is related to the complex dielectric constant ϵ by

$$\alpha(\omega) = 2Im\left(\frac{\omega\sqrt{\epsilon}}{c}\right). \tag{7}$$

In general, the complex dielectric constant is wavelength-dependent, and as a consequence $\alpha(\omega)$ is not proportional to $\kappa(\omega)$, the ratio κ/α is wavelength-dependent.

However, for dielectric dust materials in the FIR/submm range, the value of the imaginary part ϵ'' of the complex dielectric constant $\epsilon(\omega)$ is negligible with respect to the real part $\epsilon'(\omega)$

(details can be found in Paper I). This condition $\epsilon''(\omega) \ll \epsilon'(\omega)$ leads to

$$\alpha(\omega) \approx \frac{\omega}{c}\frac{\epsilon''}{\sqrt{\epsilon'}}, \tag{8}$$

and therefore:

$$\frac{\kappa(\omega)}{\alpha(\omega)} = \frac{9\sqrt{\epsilon'}}{\rho(\epsilon' + 2)^2}. \tag{9}$$

The real and imaginary parts of the complex dielectric constant are coupled through the Kramers-Kronig relations. It implies that $\epsilon''(\omega) \ll \epsilon'(\omega)$ and that the real part of $\epsilon(\omega)$ can be considered constant ($d\epsilon'/d\omega = 0$). As a consequence, the ratio $\kappa(\omega)/\alpha(\omega)$ is almost constant in the FIR/submm range, and the slopes of $\kappa(\omega)$ and $\alpha(\omega)$ are the same.

3.2. A disordered charge distribution

The disordered charge distribution (DCD) description of an amorphous material shows that in the FIR/mm wavelength range, the absorption coefficient due to acoustic lattice oscillations is temperature-independent and can be written:

$$\alpha_{DCD} = \frac{(\epsilon + 2)^2}{9}\frac{1}{3v_t^3}\langle\frac{q^2}{m}\rangle\frac{\omega^2}{c\sqrt{\epsilon}}\left[1 - \left(1 + \frac{\omega^2}{\omega_0^2}\right)^{-2}\right]. \tag{10}$$

Here, $\omega_0 = v_t/l_c$ with v_t the transverse sound velocity in the material and l_c the charge correlation length, c is the speed of light, $< q^2/m >$ the mean squared charge deviation per atomic mass, and ϵ the dielectric constant. It must be pointed out that the DCD process presents two asymptotic behaviors for the absorption and spectral index, on both sides of ω_0. The spectral index varies between 2 in the short wavelength range ($\omega > \omega_0$) and 4 in the long wavelength range ($\omega < \omega_0$). ϵ, v_t, and $< q^2/m >$ is likely to vary with material composition and with disorder at second order. In the absence of a clear identification of the material composing astronomical grains, we adopt for modeling purpose the numerical values used by Bösch (1978). The important effect for our study is the wavelength profile of the DCD absorption. As a consequence only the numerical value of ω_0 is relevant. The value of l_c will be derived from $\omega_0 = v_t/l_c$ taken the reference sound velocity equal to 3×10^5 cm.s^{-1} into account.

3.3. A two-level system

Originally, the TLS description is based on the assumption that the amorphous characteristics of the solid enables close configurations of atoms or groups of atoms, which can be described

Bin	T_{fit} (K)	F_{100} (Jy)	F_{550} (Jy)	F_{850} (Jy)	F_{1382} (Jy)	F_{2098} (Jy)	nb. compact sources/bin	Arch. name
1	8.2	25.1±3.4	434.8±66.0	86.5±15.0	15.1±3.2	3.1±0.6	29	15, 41, 48, 63, 64, 66, 73, 110,124, 132, 143, 151, 158, 188, 191, 200, 222, 231, 232, 239, 245, 247, 256, 259, 266, 272, 289, 291, 297
2	10.1	34.2±4.6	315.8±47.8	65.6±11.3	15.3±3.2	3.0±0.5	47	1, 45, 49, 51, 54, 69, 79, 87, 90, 99, 105, 106, 111, 137, 138, 139, 141, 145, 146, 150, 169, 171, 174, 175, 176, 180, 181, 186, 192, 197, 203, 204, 210, 227, 228, 240, 249, 252, 255, 267, 270, 274, 276, 284, 295, 296, 298,
3	11.9	99.6±13.4	380.9±58.5	81.9±14.4	21.9±4.6	4.7±0.8	20	17, 37, 47, 58, 62, 65, 84, 93, 116, 127, 162, 168, 196, 206, 207, 211, 220, 224, 242, 253
4	13.8	368.1±49.7	416.8±63.3	106.3±18.3	22.0±4.7	5.5±0.9	21	38, 59, 61, 76, 89, 97, 98, 109, 130, 155, 157, 160, 166, 173, 185, 189, 216, 229, 251, 260, 292
5	15.6	700.8±94.6	410.1±62.8	96.2±17.3	23.2±4.9	5.9±1.0	12	21, 35, 95, 102, 113, 118, 163, 164, 235, 237, 275, 301,
6	17.4	1960.7±264.7	573.3±88.0	145.6±25.3	29.8±6.3	8.1±1.3	9	11, 14, 112, 133, 152, 269, 277, 290, 300
7	19.3	3311.4±447.0	579.6±89.1	133.0±23.3	28.6±6.1	5.9±1.2	5	78, 92, 100, 226, 246
8	21.1	1877.5±253.5	367.3±61.2	95.5±17.9	29.9±6.5	5.6±1.3	4	5, 117, 179, 268
9	23.0	2720.0±367.2	730.0±127.3	222.0±40.6	54.2±12.0	19.3± 3.3	1	234
10	24.8	991.0±133.8	257.5±44.9	66.5±13.5	23.9±5.3	8.0±1.4	2	57, 114

Table 2. Description of the Archeops spectra bins used in this study.

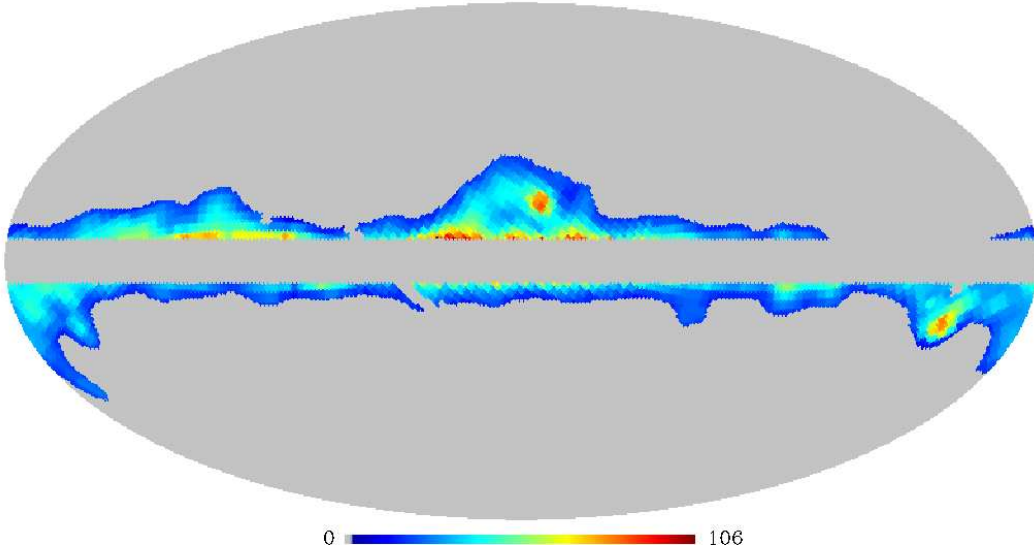**Fig. 1.** Map of the FIRAS 240 μm data used in this work ($|b| < 6°$ and $I_{240} < 18$ MJy/sr). Units are MJy/sr.

by an ADWP. The TLS model describes the interaction between electromagnetic waves and the split ground states (which represent the two-level systems) of these ADWP that are optically active; i.e. they are characterized by a non-zero dipole moment. Phenomenologically, because of the amorphous nature of the material, each ADWP is local and specific, but in a macroscopic analysis, the disorder in the amorphous material can be studied in terms of an ordered distribution of TLS with a simple density of states. Three interaction mechanisms, which all depend on temperature, can occur in such a population of TLS sites: a resonant absorption, and two relaxation processes identified as "tunneling relaxation" and "hopping relaxation". As opposed to resonant phenomena, the electromagnetic field does not cause the transition between the two energy levels for relaxation mechanisms. It means that all relaxation processes, regardless of their splitting energy $\hbar\omega$, can participate in the absorption of the electromagnetic wave of a given frequence ω_0, unlike the resonant effect where only the TLS characterized by the energy $\hbar\omega_0$ can absorb. The various effects can be described as follows:

– Resonant absorption (Hubbard et al., 2003):
The resonant absorption of a photon of energy $\hbar\omega$ concerns only those TLS characterized by the splitting energy $\hbar\omega$. Such a mechanism gives an absorption that decreases with the increasing temperature and vanishes when the temperature is high enough that the two-levels become equally populated. The resonant absorption can be written as:

$$\alpha_{res} = \frac{4\pi^2}{3c\sqrt{\epsilon}} \frac{(\epsilon+2)^2}{9} \omega G(\omega) \tanh(\hbar\omega/2kT_d), \quad (11)$$

where k is the Boltzmann constant, ϵ the dielectric constant, and $G(\omega)$ the optical density of state (ODOS). For simplicity, and to compare our results with a reference, we follow Bösch (1978) and consider a constant ODOS, i.e. $G(\omega) = G_0$, with G_0 equal to 1.4×10^{-3} (CGS units).

– Tunneling relaxation:
In terms of absorption, this process occurs when the phonon energy is too low to allow direct transitions above the bar-

rier height between the two levels. In this case, additional tunneling is required to perform the transition. The tunneling absorption increases with temperature. We derive the following accurate and relatively simplistic expression for the phonon-assisted tunneling absorption, more convenient for computation than the formula obtained by Fitzgerald et al. (2001a,b):

$$\alpha_{phon} = \frac{G_0}{3c\sqrt{\epsilon}} \frac{(\epsilon+2)^2}{9} \omega \, F_2(\omega, T_d), \tag{12}$$

$$F_2(\omega, T_d) = \tag{13}$$
$$= \frac{1}{2kT_d} \int_0^\infty \int_{\tau_1}^\infty \sqrt{1 - \frac{\tau_1}{\tau}} \, \mathrm{sech}^2(\frac{E}{2kT_d}) \frac{\omega d\tau dE}{1+\omega^2\tau^2},$$

where τ_1 is the relaxation time defined by $\tau_1 = a E^{-3} \tanh(E/2kT_d)$. A reasonable value for a is 4.2×10^{-56} erg^3 s (in the case of soda-silica glass; Bösch, 1978).

– Hopping relaxation:
Hopping relaxation occurs when the phonon energy allows a direct jump above the barrier. It gives an absorption that increases with temperature:

$$\alpha_{hop} = \frac{8\pi}{3c\sqrt{\epsilon}} \frac{(\epsilon+2)^2}{9} G_0(c_\Delta + lnT_d) \int_0^\infty dV P(V) \frac{\omega^2\tau}{1+\omega^2\tau^2} \tag{14}$$

where τ is the relaxation time defined by $\tau = \tau_0 \exp(V/T_d)$. For amorphous silica, $\tau_0 \simeq 1 \times 10^{-13}$s (Bösch, 1978). c_Δ, an additional parameter of tunneling states is given by

$$c_\Delta = ln\frac{k_B}{\Delta_0^{min}} + ln4 - 1 + \int_0^1 ln\, arctan(x)\, dx \tag{15}$$

where Δ_0^{min} is the minimal energy splitting. Only a lower limit of c_Δ with a value close to 5.8 has been determined from laboratory experiments. P(V) is the distribution of the TLS barrier height which can be approximated by

$$P(V) = C_V p_v(V) \text{ with} \tag{16}$$

$$C_V \cong \frac{1}{V_0\sqrt{\pi}}, \text{ and} \tag{17}$$

$$p_v(V) = \begin{cases} \exp(-(V-V_m)^2/V_0^2) & \text{for } V > V_{min}, \\ 0 & \text{for } V < V_{min}, \end{cases} \tag{18}$$

such as $V_{min} = 50$ K, $V_m = 550$ K and $V_0 = 410$ K.

All physical parameters are set to the values from Bösch (1978), and are provided in Table 3. The amplitude of the TLS processes with respect to the DCD part is controled by a relative intensity parameter denoted A (see Section 3.4). The total absorption (α_{tot}) deduced from the TLS model is the sum of all the processes quoted in this section:

$$\alpha_{tot} = \alpha_{DCD} + A \times (\alpha_{res} + \alpha_{phon} + \alpha_{hop}). \tag{19}$$

3.4. Model parameters

The relevant parameter for the DCD absorption is the charge correlation length l_c, which controls the wavelength where the inflection point between the two asymptotic behaviors with $\beta = 2$ and $\beta = 4$ occurs. The relative amplitude between the DCD and the TLS effects is not strongly constrained by the model prior to
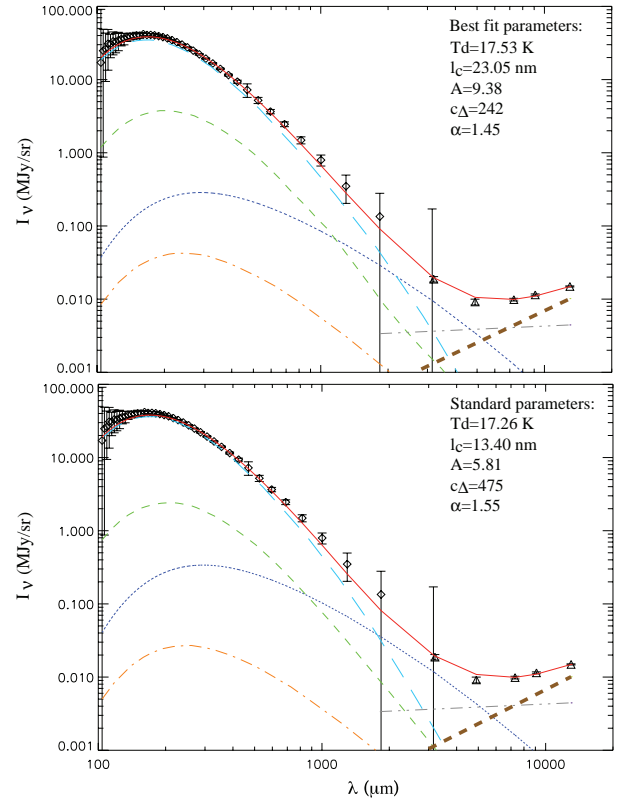

Fig. 2. FIRAS/WMAP diffuse MW spectrum fitted using the TLS model: total in red (solid), DCD process in light blue (long dash), and TLS processes: resonant absorption in green (**dash**), hopping relaxation in dark blue (dot), and tunneling relaxation in orange (dash-dot), with the best-fit parameters (top panel) and standard parameters (bottom panel). The gray line (dash-dot-dot-dash) corresponds to free-free emission, and the brown line (thick dash) to a λ^α power law.

the comparison with astrophysical data. The factor that controls the amplitude of the DCD absorption depends on the characteristics of the material, whereas the amplitude of the TLS effects (resonant, tunneling, and partly hopping) is related to the TLS density of states. Therefore, to simply characterize the relative importance of the TLS and the DCD processes, we use a single free parameter of relative intensity denoted A. This means that all TLS effects are multiplied by the same intensity A (see Eq. 19). The respective contributions of the resonant and of the two relaxation processes are set according to theory. The resonant effect and tunneling relaxation correspond to a quantum tunneling effect. However, the hopping relaxation is a more classical effect, since there is no tunneling involved. The characteristics of the potential wells to be taken into account in computing the absorption in case of hopping or tunneling are different, depending on the classical or quantum tunneling process. Therefore, we want to keep the possibility of uncoupling these effects, by means of the c_Δ coefficient. The dust temperature can be derived from the shape of the dust SED in the FIR and also controls the amplitude of the TLS relaxation effects. It is therefore a crucial parameter of the model, linking the FIR emission to the submm behavior of the optical properties of dust.

Finally, we adopt the following four free parameters for the TLS model in this study: T_d, l_c, A, and c_Δ. Note that these parameters allow only to characterize the shape of the emission.

v_t^* (cm/s)	$<q^2/m>^*$ erg.cm.g^{-1}	$\epsilon^{*\dagger}$	$G_0^\dagger$ (CGS units)	$a^\dagger$ (erg^3.s)	$\tau_0^\dagger$ (s)	$V_0^\dagger$ (K)	$V_m^\dagger$ (K)	$V_{min}^\dagger$ (K)
3×10^5	8748	2.6	1.4×10^{-3}	4.2×10^{-56}	10^{-13}	410	550	50

Table 3. Physical parameters used in the TLS model.
* defined in Section 3.2.
† defined in Section 3.3.

One additional parameter is required to set the overall amplitude of dust emission. Classically this is done by assuming a dust/gas ratio and some dust emissivity at a given reference frequency. Also, the number of free parameters used here is roughly the same as the one needed to achieve a description of the emission shape with the FDS model (α_1, α_2, T_2, q_1/q_2, and f_1).

4. Comparison with astrophysical data

4.1. Determination of the best-fit parameters

The diffuse medium sampled by the FIRAS/WMAP SED and the compact sources detected in the Archeops data could exhibit rather different dust properties. In a first step, we therefore model the two datasets separately, in order to illustrate possible differences between the two environments. However, as explained in Section 2.2, only the Archeops data sample the range of temperature needed to constrain the TLS model. We also therefore perform a combined fit where all data are used, in order to derive standard parameter values allowing both diffuse medium and compact sources to be reproduced. In each case, we proceed in the same way, i.e., we use the idl "mpfit" function to perform a χ^2 minimization between the observational data and the TLS model. Results of the minimization are given in Table 4. The prediction of the model is color-corrected to match the observation in the large photometric filters of each instrument.

4.1.1. Modeling of the FIRAS/WMAP MW spectrum

The model has been compared with the FIR/mm SED of the diffuse MW emission. For the longest wavelengths, dust emission is not the main contributor, in particular in the WMAP bands. We take free-free emission into account using the free-free template at 30 GHz constructed by Dickinson et al. (2003), derived from the Hα map, and extrapolated in frequency using a power law for the specific intensity with $I_\nu \propto \lambda^{0.1}$. In addition to the free-free emission, we have incorporated a power law emission that can describe synchrotron emission, probably mixed with other types of emission such as spinning dust. The slope of this power law (α) is left as a free parameter, since contamination in this wavelength range is not well known. The brightness level of the free-free combined with the power law emission has been normalized to the 23 GHz data. Figure 2 (top panel) shows the result of the modeling. From Table 4 we can see that the dust temperature is robustly derived, and the value of 17.5 K is similar to the results of Boulanger et al. (1996), who analyzed the emission in the solar neighborhood. However the other parameters are not well constrained using only the FIRAS/WMAP SED. The A parameter controls the intensity of all TLS effects, whereas the c_Δ parameter allows us to increase/decrease the emission coming from the hopping relaxation. To reproduce only the mm flattening in the spectrum deduced from the FIRAS data, the model requires an increase in the emission in the submm domain, which can be explained by an increase of either A or c_Δ. These two

parameters are therefore highly degenerate in this fit configuration. The 1-σ uncertainty on the correlation length indicates that using only the FIRAS/WMAP data is not sufficient for constraining this parameter, which controls the slope of the emission spectrum. Indeed, changing l_c is equivalent to modifying the apparent emissivity spectral index β, and β is known to be naturally anticorrelated with dust temperature. Therefore, the only way to constrain this parameter is to compare the model to spectra at various temperatures, which means that the modeling of the Archeops spectra is important to derive l_c (see Section 4.1.2). The specific intensity is best fitted by a power law of the form $I_\nu \propto \lambda^\alpha$ with $\alpha = 1.45$. Variations in the synchrotron index have been found in our Galaxy with values ranging from 0.6 in star-forming complexes to 1.2 in the interarm regions. Our value is higher than the observed α values for synchrotron alone, which could indicate that this emission is not only due to synchrotron emission, but may also include a significant contribution from spinning dust emission. Although spinning dust emission has not been shown at high latitude, some studies indicate that it is widespread in the Galaxy (Miville-Deschênes & Lagache, 2005; Planck collaboration, 2011d).

4.1.2. Modeling of the Archeops spectra

In this section, we perform the minimization on the Archeops spectra, averaged in ten temperature bins. The IRAS 100 μm data were also included in the spectra. Since the wavelength domain is limited to $\lambda \simeq 2$ mm, no free-free or spinning dust emission were included in the fits. For each set of parameters [l_c, A, c_Δ], the model is computed for temperatures between 5 K and 35 K, with a step of 0.5 K, and adjusted to the spectra for the best dust temperature for each spectrum, by looking for the lowest χ^2 value. Therefore, we determine the best set of parameters that is able to reproduce all Archeops spectra by only changing the dust temperature. Results of the minimization are presented in Figure 3 and Table 4. A comparison between the temperature derived from a modified black-body fit (Désert et al., 2008) and the temperature deduced from the TLS model are also given in Figure 3. Whereas a modified black-body fit samples the range 8.2-24.8 K, the TLS model shows temperatures from 10 to 17.5 K. This discrepancy is essentially due to the mm excess which can bias the temperature determination when using a modified black-body fit. In Section 5.3, we discuss the temperature estimates depending on the method used.

The parameters are better constrained than in Section 4.1.1, with lower 1-σ uncertainties, especially for l_c with a value of 5.11±0.09 nm. In Figure 3 we can see that the flattening of the spectra with increasing dust temperature (from top to bottom panels, and from left to right) is mostly consistent with the hopping relaxation process. However, the spectra with the lowest dust temperature indicate that the Archeops data at longer wavelengths and at 2 mm in particular, show a resonant absorption on the same order of magnitude or higher than implied by the hopping relaxation process. Also, we note that the tunneling
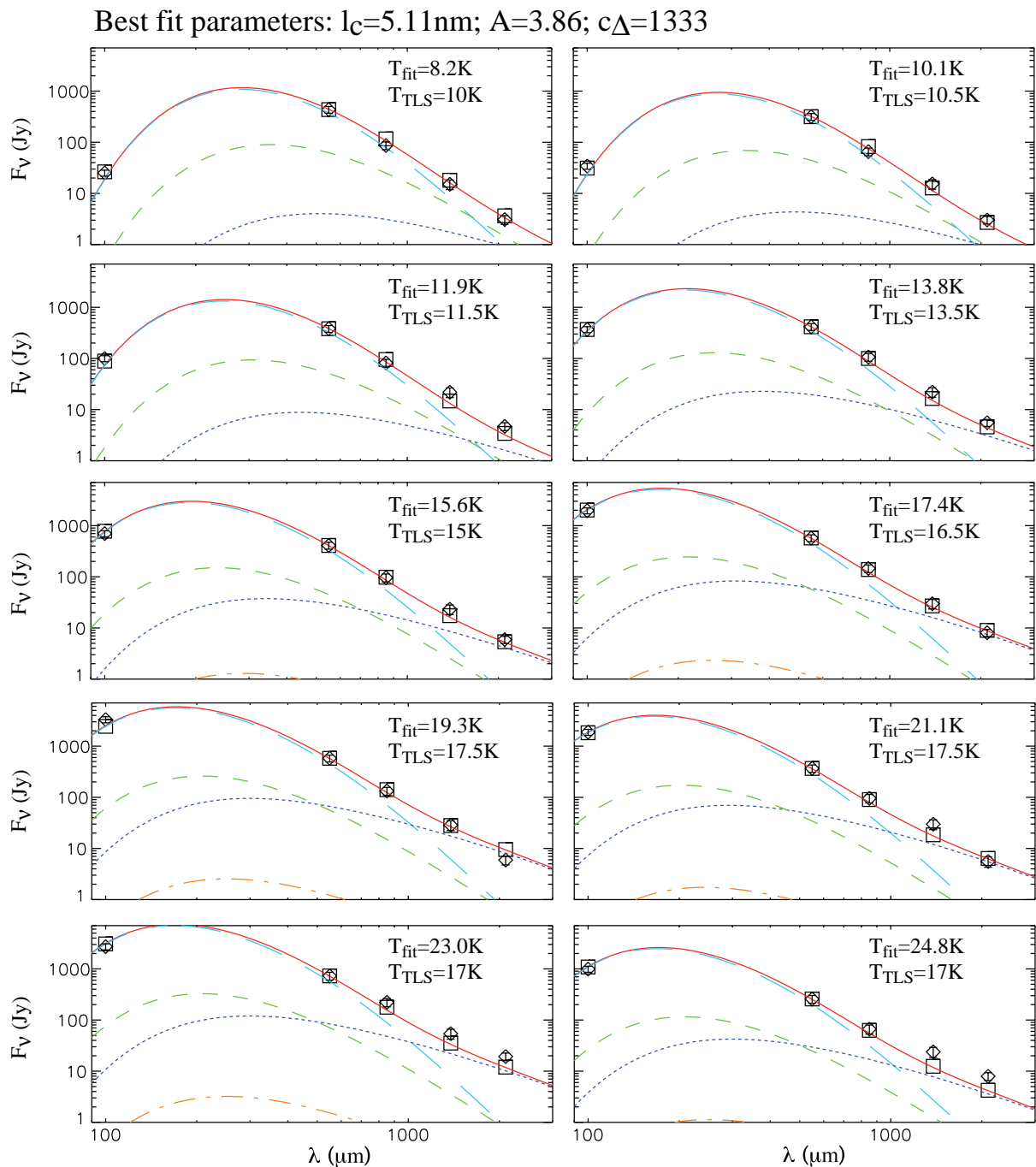
Fig. 3. Spectra of Archeops compact sources (diamonds), binned in temperature, fitted using the TLS model, with the best-fit parameters (this page) and the standard parameters (next page). The contribution of the different processes is given in the caption of Figure 2. Squares correspond to the model after color correction. The average temperature per bin deduced from a single modified black-body fit (from Désert et al.,2008), and the temperature deduced from the TLS model are given in the top right of each panel. The description of the Archeops spectra is given in Section 2.2 and in Table 2.

relaxation contribution is much lower than the other processes. The minimization of Galactic compact sources favors a lower intensity of the TLS resonant process which results in the increase in the amplitude of the hopping relaxation, as compared to the modeling of the FIRAS/WMAP spectrum. In other words, the decrease in the A parameter requires a higher value of c_Δ.

4.1.3. Modeling of the FIRAS/WMAP and Archeops spectra

To derive general properties of Galactic dust, we performed a combined fit of the diffuse medium and compact sources SEDs. Best-fit parameters, denoted "standard" parameters are given in Table 4. Figures 2 and 3 also show the results of the modeling when using the standard parameters. Since the dust temperature is only derived from the FIRAS/WMAP SED, we would expect a similar value as in the combined fit. However, because
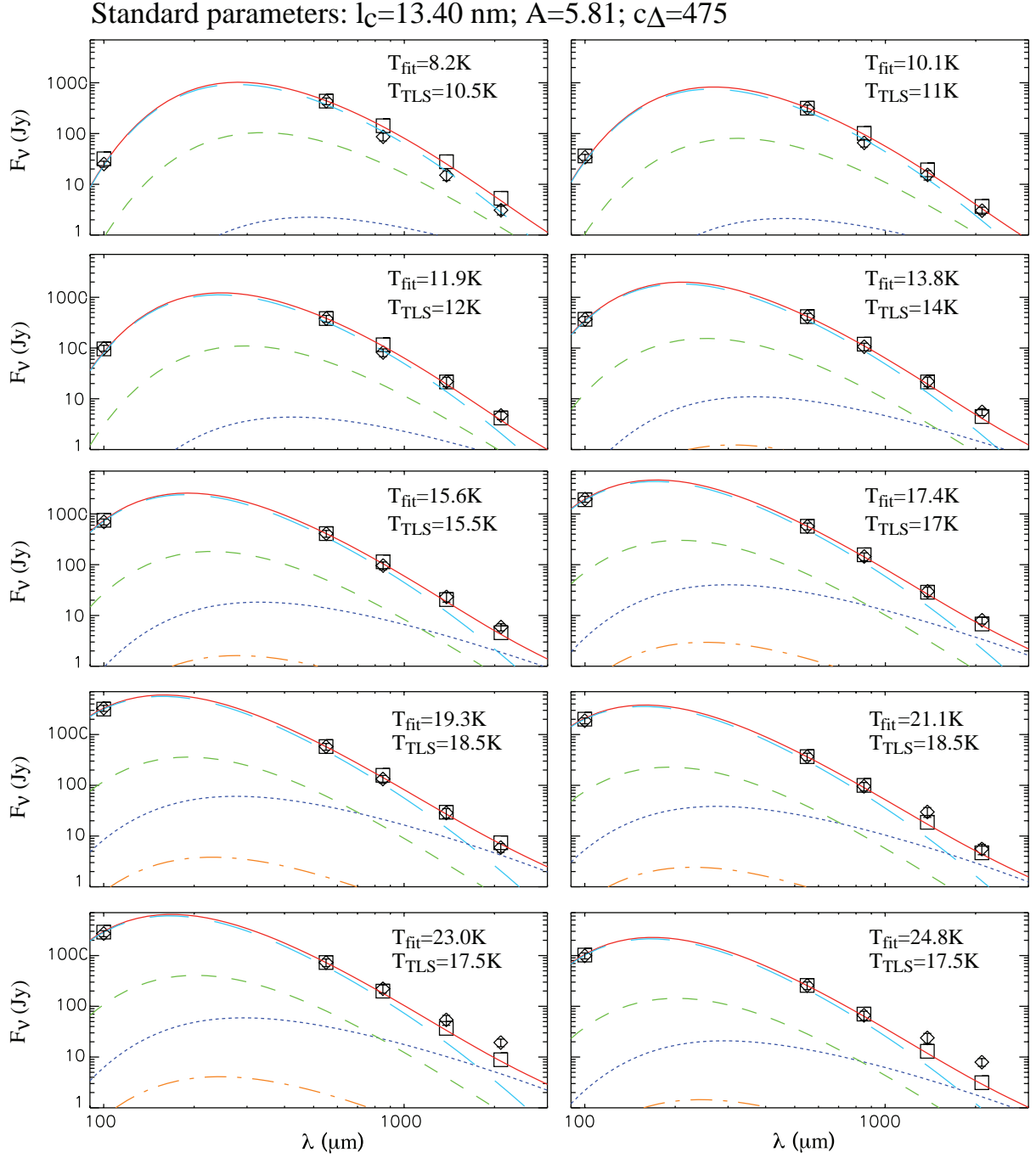
Standard parameters: l_C=13.40 nm; A=5.81; c_Δ=475

Fig. 3. Continued.

the FIR spectral shape of the BG emission also depends on l_c, changes in l_c produce changes in T_d, since the two parameters are degenerate. We note a decrease in l_c with a value of 13.4 nm, compared to the value derived using only the diffuse medium emission (l_c = 23.05 nm). This explains that the best temperature estimate (T_d = 17.26 K) does not fully match the value obtained when fitting only the FIRAS/WMAP data (T_d = 17.53 K). Actually, the l_c, A, and c_Δ parameter values are intermediate, compared to the values obtained when fitting independently the diffuse medium emission on one side and compact sources on the other. We note that using the same set of TLS parameters for all Archeops compact sources does not reproduce the long

wavelength data well in the case of the warmest spectra as determined by a modified black-body fit (T_{fit}=23.0-24.8 K.). In that case, the TLS model underestimates the brightness at 1382 and 2098 μm.

In Figure 2 we do not see any significant difference in the modeling of the FIRAS/WMAP spectrum when using the best-fit or standard parameters. However, when looking at Figure 3, the use of the standard parameters has some non-negligible effects on the fit modeling. For instance, the fitting of the coldest spectrum shows an overestimate of the brightness at long wavelengths, which was not the case with the best-fit parameters. Also, the warmest spectra are described less well

Table 4. Parameters of the TLS model.

	T_d (K)	l_c (nm)	A	c_Δ	α	reduced χ^2
Galactic diffuse emission (FIRAS/WMAP)						
Parameters	17.53	23.05	9.38	242	1.45	1.95
1-σ	± 0.02	± 22.70	± 1.38	± 123	± 0.15	–
Galactic compact sources emission (Archeops)						
Parameters	–	5.11	3.86	1333	–	1.45
1-σ	–	± 0.09	± 0.13	± 68	–	–
Galactic diffuse and compact sources emission						
Standard parameters	17.26	13.40	5.81	475	1.55	2.53
1-σ	± 0.02	± 1.49	± 0.09	± 20	± 0.11	–

when adopting the standard parameters. This could indicate that dust properties are different in the diffuse medium observed with FIRAS/WMAP and in compact sources observed with Archeops.

4.2. Discussion of fit results

Parameters giving the best match between the TLS model and the Galactic emission spectra correspond to a dust temperature of T_d =17.26 K, a correlation length close to l_c =13 nm, an intensity of the TLS processes with respect to the DCD one of about A =6, and an intensity parameter for the hopping relaxation of c_Δ =475. The dust temperature characterizing the diffuse interstellar medium is quite close to the value of 17.5 K derived by Boulanger et al. (1996) at high Galactic latitudes. We note that the correlation length is within the same order of magnitude as the minimal size of the smallest grains in the BG population. The largest grains could result from aggregation of grains with a size close to the correlation length. The value of the A parameter is reasonable considering the paucity of quantitative experimental data in this field (essentially Bösch, 1978). In solid-state physics, the phenomenology of these effects is different, and these effects could result from distinct types of disorder in the material. The moderate value found for the parameter A indicates that the relative intensity of the DCD and TLS processes has the same order of magnitude as in the case studied by Bösch (1978).

For the physical properties related to defects in the grain material, the measured values of defect concentration and induced defects can easily vary over several orders of magnitude. Therefore the derived A value suggests a similar origin for the DCD and TLS processes, and therefore justifies the use of a similar density of state. The value of c_Δ is significantly higher than the minimum value of 5.8 deduced from laboratory experiments, at low temperature. Once again, in a material with a known chemical composition, the magnitude of the physical effects caused by defects in the material are likely to vary over several decades. The value derived from observational data is in that sense fully acceptable. This value indicates that the hopping relaxation is more efficient than the two other TLS processes, related to tunneling and therefore highly dependent on the distance between the two potential minima of the TLS. However, we note that each TLS process is characterized by its own emission profile, dependent on the parameters for each site. For instance, modifying V_m, V_0, and V_{min} would induce variations in the emission profile of the hopping relaxation effect. As a consequence the c_Δ value would have to be modified.

5. Model predictions

5.1. Spectral shape evolution with temperature - Emissivity spectral index

In Figure 4, we present the predicted model SED evolution using the standard parameters taken from Table 4 for different dust temperatures. The resonant absorption and the hopping relaxation process have different behaviors with temperature: the hopping relaxation increases with increasing temperature, whereas the resonant absorption decreases. The tunneling relaxation can be neglected over the range of temperature explored here, since it appears to be systematically dominated by one of the other TLS processes, and does not induce any specific variations in the dust emission spectrum. The millimeter excess emission, as well as the flattening of the spectrum with temperature, is mainly produced by the hopping relaxation. As a consequence, the excess increases with temperature, and the transition between the DCD and TLS processes shifts towards shorter wavelengths with increasing temperature since the intensity of the hopping relaxation increases.

One of the most important aspects of the TLS model to be explored is the variation in β with temperature. We compared the TLS to the FDS model number 7 (see Table 2 in Finkbeiner et al., 1999). The same method has been applied to each model. We generated a set of emission spectra for temperatures between 10 and 35 K corresponding to temperatures derived using the TLS model (hereafter T_{TLS}) in one case, and to the warm component (T_2) of the FDS model, which is related to that of the cold component (see Eq. 14 in Finkbeiner et al., 1999), in the other. Each spectrum has been integrated in the IRAS 100 μm and Archeops photometric bands to produce simulated SEDs. We then fitted these fake SEDs at different temperatures by a single modified black body (T_d-β fit), assuming the same absolute uncertainties as for the actual IRAS and Archeops data (see Section 2.2). Results of the T_d-β fits are presented in Figure 5. The TLS model clearly highlights an inverse relationship between the spectral index and the temperature of the fit (hereafter T_{fit}) in agreement with the dust behavior in Désert et al. (2008), whereas the FDS model shows the opposite behavior, i.e. an increase in β with temperature. We also note that the FDS model is not able to predict β values higher than 1.6 in the wavelength range observed with Archeops. Using standard parameters, the TLS model predicts β variation between 2.3 and 1 in the wavelength domain going from 100 μm to 2 mm, for T_{fit} between 10 and 70 K.

Models such as the FDS model, which do not exhibit any intrinsic variation in the apparent spectral index with temperature may still explain the obervations in principle, provided an

adequate temperature mixing along th LOS or within the beam sufficiently alters the emitted SED.

First, we note that, since temperature mixing can only broaden the emitted SED, the intrinsic β should be larger than the range of observed ones. Since many of the Archeops point sources and Planck cold cores (Planck collaboration, 2011e) have apparent β larger than 3-4, this would require a model with a very steep intrinsic β value. Apart from the TLS model proposed here, which can produce this steep behavior under specific circumstances, there has been no proposal for dust models that allows such high β values.

Second, the effect of temperature mixing has been analyzed in several studies. Malinen et al. (2011), for instance, have investigated this effect through 3D MHD simulation, taking both full radiative transfer and a dust model with no intrinsic β variations into account. They considered both cases, with and without embedded stars heating the surrounding ISM, assuming reasonable luminosity and spatial distribution for the sources. Paradis et al. (2009) studied the emissivity variations induced by an ISRF strength mixture using the Dale et al. (2001) concept of a power-law distribution of dust mass subjected to a given heating intensity ($dM_d(X_{ISRF} \propto X_{ISRF}^{-\alpha} dX_{ISRF}$). The α parameter has been tuned in the range $\alpha=1$ (active star-forming regions) up to $\alpha=2.5$ (diffuse medium). Both methods give similar results.

For cases with no embedded source, temperature mixing can reproduce neither strong wavelength-dependent variations in the emissivity nor the spread of β values observed. Indeed, Malinen et al. (2011) show that the model corresponding to that case actually produces a weak correlation between T_d and β, which is the opposite of the anticorrelation that is observed. In cases of star-forming regions, when discrete stellar heating is included in the Malinen et al. (2011) model, most LOS in their simulation show a similar correlation trend. However, those LOS towards discrete objects (which corresponds to Dale's α-parameter $\simeq 1.25$ in Paradis et al., 2009) present a wavelength-dependent variation in emissivity, leading to an apparent T_d-β anticorrelation with a shape similar to what is observed toward some regions. Those map pixels affected by temperature-mixing around heating sources, however, have apparent temperatures higher than 14 K following Malinen et al. (2011) and, as already pointed out, β values always lower than the ones characterizing the SEDs without temperature mixing.

As shown in Table 2, most of the Archeops point sources considered here have temperatures lower than 14 K, down to 8 K, and high spectral index values. This shows that they are most likely not affected by temperature mixing and are actually closer to cold cores, as detected in the Planck data (Planck collaboration, 2011e). It is there observed that such sources exhibit narrow SEDs. For a single dust temperature along the LOS, their narrowness is only compatible with spectral index values higher than 3. And a strong distribution of temperature would require still higher spectra index values to fit the observed SEDs. For the above reasons, we do not favor a model without intrinsic β variations and temperature mixing along the LOS to simultaneously explain the diffuse MW SED and the Archeops point sources, and propose that the TLS model with the parameters derived here could reasonably explain both.

To extend the analysis on the β variations, we present in Figure 6 how the predicted β changes as a function of both temperature and wavelength, computed as $dln\epsilon_e/dln\lambda$. For temperatures below 15 K, the spectral index is expected to exceed 2 and reach 2.6 at T_d=10 K, around 2 mm. Then β decreases with increasing wavelength and gets as low as 0.5 at longer wave-
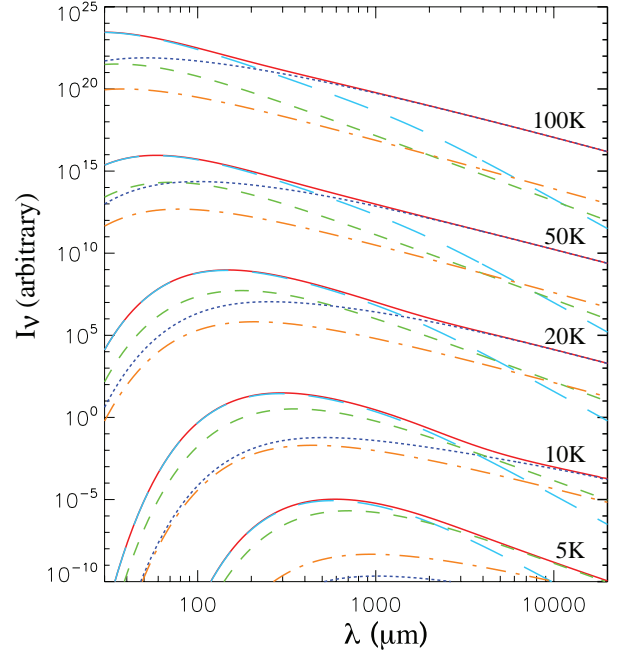

Fig. 4. Prediction of the FIR/mm emission at different temperatures, deduced from the TLS model using standard parameters (see Table 4). The contribution of the different processes is given in the caption of Figure 2.

lengths, where dust emission is usually dominated by other emissions such as free-free and synchrotron. Temperatures higher than 20 K and 100 K lead to β values less than 2 and 1.7 at $\lambda > 100$ μm, respectively. We note that at 2 mm, in the range 10-40 K, the spectral index roughly varies from 2.6 to 1. To summarize, the β values predicted by the TLS model vary strongly both with wavelength and dust temperature.

In Figure 7 we show the evolution of β in three ranges of wavelengths ([100 μm-2 mm], [100-550 μm] and [550 μm-2 mm]) for different couples of the parameters [A, l_c]. The c_Δ value is fixed to the standard value of 475. For a given β and temperature, one can estimate the correlation length of the dust grains, as well as the intensity of the TLS effects. Regardless of the value of the parameters, Figure 7 highlights a decrease in β with temperature going from 10 to 55 K for most [A, l_c] couples. The β variations are more pronounced as A increases. The behavior of β with temperature does not change for $l_c \geq 30$ nm, regardless of the A value. In that case, the DCD part has reached the asymptotic behavior in λ^{-2}, and only the TLS effects can induce a decrease in β with T_d. Low values of l_c associated with low values of A produce the highest β values, which can reach β=3.4-3.5 at low temperatures in the three wavelength ranges. The DCD asymptotic behavior in λ^{-4} has not been reached in Figure 7, since the TLS effects never vanish completely and l_c values around 0.1 nm would be required, which is not realistic since the interatomic distance is $\simeq$0.2-0.3 nm range. High values of A induce low values of β at high temperatures. The value of β can be as low as 0.55 between 550 μm and 2 mm, for temperatures higher than 25 K, in case of $A = 10$ and $l_c = 1$ nm. The same values of A and l_c, however, reproduce $\beta \simeq 1.4$, for T_d=55 K in the range 100-550 μm.
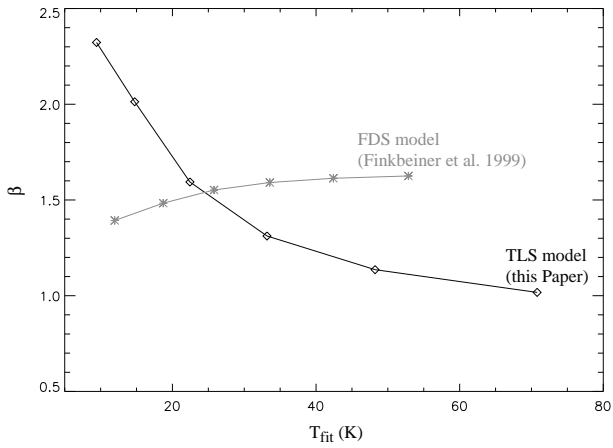
Fig. 5. Prediction of the emissivity spectral index as a function of temperature, deduced from a modified black-body fit on emission spectra at various temperatures, in the IRAS 100 μm and Archeops bands. The emission spectra have been generated using the TLS (black) (using standard parameters, see Table 4) and FDS (gray) models.
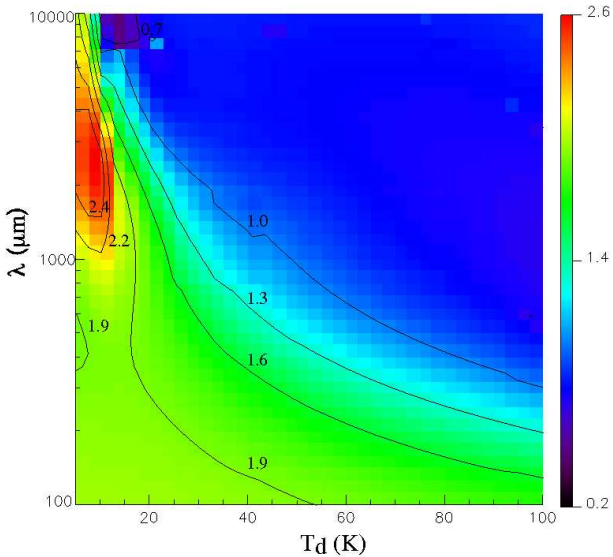

Fig. 6. Prediction of the emissivity spectral index deduced from the TLS model using standard parameters (see Table 4), as a function of wavelength and temperature, with overplotted contours.

Fig. 7. Prediction of the emissivity spectral index in the range [100 μm-2 mm] (top panel), [100-550 μm] (middle panel), [550 μm-2 mm] (bottom panel), deduced from the TLS model as a function of dust temperature, for different parameter couples [A, l_c (nm)] assuming $c_\Delta = 475$.

5.2. Dust emissivity

One of the most important aspects of a given FIR/mm dust emission model is to predict the dust emissivity and its variations with wavelength and temperature. This point is pivotal both for inferring gas masses and for separating foreground emission from the cosmic microwave background (CMB). Here, we quantify how adopting the predictions of the TLS model affects the dust mass determination obtained from FIR and submm measurements. The reference emissivity value is 1×10^{-25} cm^2/H at 250 μm in the solar neighborhood (Boulanger et al., 1996). This value has been derived for a dust temperature of 17.5 K. Besides variations with wavelength, the TLS model predicts variations with temperature. We impose the model to recover the Galactic emis-
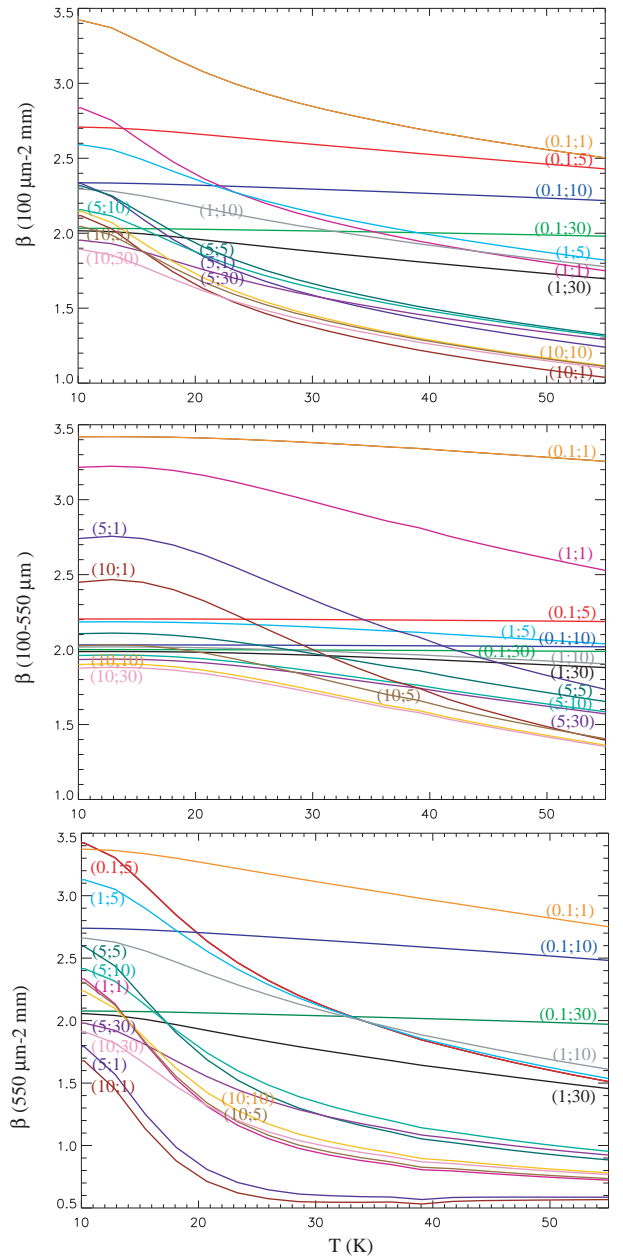
sivity reference at 250 μm from Boulanger et al. (1996), for a temperature of 17.5 K. Emissivity predictions have been integrated for different temperatures in the IRAS, Herschel PACS and SPIRE, Planck HFI and LFI channels. The color correction has then been applied to each instrument. Values of the predicted emissivities are given in Table 5. Figure 8 shows the emissivity predictions for temperatures between 5 K and 100 K, overlaid with a λ^{-2} power-law emissivity. We note that between 5 and 17 K, the emissivity variations follow a λ^{-2} power law in the range 100 μm-1 mm. At higher temperatures, the emissivity spectra become flatter than a modified black-body with $\beta=2$, starting in the FIR domain and flattening even more with wavelength. We observe that emissivities at 5 and 10 K only differ for $\lambda > 4$
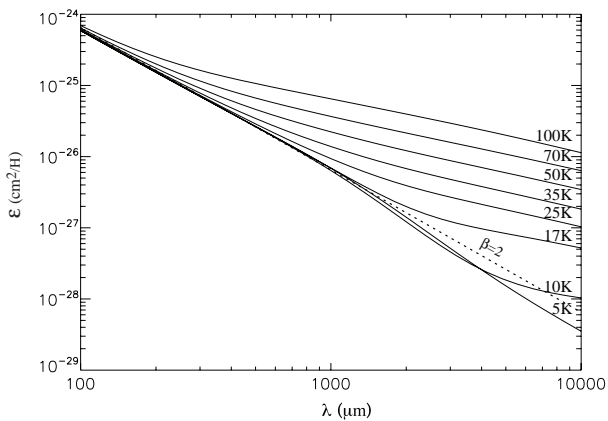
Fig. 8. Predicted emissivity with the TLS model using the standard parameters given in Table 4, as a function of wavelength for different temperatures. The dashed line shows a λ^{-2} emissivity power law for comparison.

mm. For $T_d > 10$ K, we can see that the difference between the curves increases significantly with wavelength and temperature. Whereas the discrepancy between predictions at 5 K and 100 K is about a factor 2 at 250 μm, it is about a factor 35 at 2 mm, and $\simeq 100$ at 4 mm.

Therefore, when assuming no dependency of the emissivity spectrum with either wavelength or temperature, one can significantly bias the mass estimate, especially when derived from submm/mm data and extrapolated to shorter wavelengths. Indeed, when assuming an emissivity decrease in λ^{-2} in the submm/mm domain, one would overestimate the dust temperature and underestimate the emissivity in the FIR, and therefore would overestimate the dust mass. For instance, this is the case for those SMC molecular clouds whose masses have been derived from mm data and found to be systematically higher (twice on average) than virial masses (Bot et al., 2007).

5.3. Temperature estimate

Dust temperature is often derived using a modified black-body fit with T_d and β taken as free parameters, or with β set to a fixed value. The latter temperature does not necessarily equal the physical temperature obtained using the TLS model, as already discussed in Section 5.1. In particular, the temperature deduced from a T_d-β fit is highly dependent on the wavelength range considered. To compare the fitted temperature with the physical one, we first generated several emission spectra at different temperatures between 10 and 60 K using the TLS model. We then integrated the TLS model predictions in the IRAS 100 μm band (crucial for estimating the dust temperature), Herschel PACS 160 μm, and SPIRE 250, 350, and 500 μm bands. We then fitted each spectrum using a least-square fit method. We also performed the analysis by integrating the TLS model in the IRAS 100 μm channel, and Planck HFI 350, 550, and 850 μm bands (857, 545, and 353 GHz), before fitting the spectrum with a modified black-body model. For both cases (IRAS-Herschel bands and IRAS-Planck bands) we have also made the test using a T_d-β fit with $\beta = 2$. For each band, we took the calibration uncertainties into account, i.e. 13.5% for IRAS (absolute uncertainty of the new generation of IRAS maps Miville-Deschênes & Lagache, 2005), 20% for PACS, 15% for SPIRE, and 7% for HFI. The relationship between the dust temperature derived using the TLS model and the T_d-β fit is modeled using a polynomial function, such as

$$T_{TLS} = \sum \gamma_n T_{fit}^n. \tag{20}$$

The best polynomial coefficients derived from a fit are given in Table 6.

The comparison between the temperature estimates is shown in Figure 9. The behavior varies significantly when deriving the temperature in the 100-500 μm range, or in the 100-850 μm range, and whether a free β is used. Up to 25 K, we observe good agreement between T_{TLS} and T_{fit}, no matter which model is used, whereas it is not the case for higher temperatures. When using a fixed (free) β, T_{fit} is systematically lower (larger) than T_{TLS}. Also, the discrepancy between the temperatures is greater when enlarging the wavelength domain to derive T_{fit}, and when β is left as a free parameter. This result highlights that the longest wavelengths ($\lambda > 550$ μm) should not be used to determine the dust temperature from a single modified black-body fit, since they are affected by significant submm/mm emission excess in the TLS model. In addition, one should be careful when using a T_d-β fit, especially when β is a free parameter of the fit, and for $T_{fit} > 25$ K. In that case, Equation 20 and Table 6 should be used to derive the actual physical dust temperature from a temperature deduced from a T_d-β fit.

We note that if the temperature estimate is performed on a wavelength range that extends up to 2 mm, as is the case when using the Archeops data for instance, the discrepancy between T_{fit} and T_{TLS} is shifted, and roughly starts and increases for temperatures over 18 K, instead of 25 K (see temperatures presented in Figure 3).

6. Discussion

One important aspect of dust emission is to be able to subtract the foreground emission. According to the TLS model, emission from large ISM grains made of amorphous material is significantly more complicated than predicted by a single modified black-body emission with a single emissivity index β. Actually, the model predicts emissivity index variations as a function of both temperature and wavelength. Therefore, within the framework of this model, it is important to take into account both dependences for component separation. Extrapolation of emission from the FIR to mm wavelengths with a single modified black body with a constant β could produce a wrong estimate of dust emission in the CMB wavelength domain. The above variations are strictly related to the amorphous nature of the material composing the grain, and should not be mistaken with variations that can result, for instance, from modifications of the grain structure, such as changes in the grain size or dust aggregation (Stepnik et al., 2003; Paradis et al., 2009), which can occur in dense regions of the ISM.

However, we caution the reader that the interpretation of the model prediction may become inaccurate when high temperatures ($\simeq 100$ K) are concerned. Indeed, in the current version of the TLS model, only the fundamental energy of the TLS states is considered, and the model requires improvement by adding the effect of excited states in the two-level systems (Gromov et al., 2011).

The TLS model predicts a wavelength and temperature dependence of the spectral index that characterizes the emission and absorption properties of the amorphous dust in the FIR and mm range. Coming from solid states physics, it should apply with a high degree of universality to all amorphous materials.

Photometric bands	IRAS	PACS	SPIRE	SPIRE	HFI	SPIRE	HFI	HFI	HFI	HFI	HFI	LFI	LFI	LFI
5 K	6.51×10^{-25}	2.55×10^{-25}	1.06×10^{-25}	5.54×10^{-26}	5.36×10^{-26}	2.85×10^{-26}	2.38×10^{-26}	1.02×10^{-26}	3.64×10^{-27}	1.23×10^{-27}	5.44×10^{-28}	2.24×10^{-28}	7.84×10^{-29}	2.88×10^{-29}
10 K	6.51×10^{-25}	2.55×10^{-25}	1.06×10^{-25}	5.53×10^{-26}	5.35×10^{-26}	2.81×10^{-26}	2.35×10^{-26}	9.73×10^{-27}	3.27×10^{-27}	1.06×10^{-27}	4.83×10^{-28}	2.35×10^{-28}	1.33×10^{-28}	9.25×10^{-29}
17 K	6.52×10^{-25}	2.56×10^{-25}	1.07×10^{-25}	5.56×10^{-26}	5.38×10^{-26}	2.83×10^{-26}	2.37×10^{-26}	1.01×10^{-26}	3.95×10^{-27}	1.82×10^{-27}	1.24×10^{-27}	9.24×10^{-28}	6.77×10^{-28}	4.56×10^{-28}
25 K	6.55×10^{-25}	2.58×10^{-25}	1.09×10^{-25}	5.78×10^{-26}	5.59×10^{-26}	3.07×10^{-26}	2.61×10^{-26}	1.27×10^{-26}	6.26×10^{-27}	3.64×10^{-27}	2.72×10^{-27}	2.03×10^{-27}	1.40×10^{-27}	9.01×10^{-28}
35 K	6.62×10^{-25}	2.64×10^{-25}	1.15×10^{-25}	6.35×10^{-26}	6.15×10^{-26}	3.63×10^{-26}	3.16×10^{-26}	1.76×10^{-26}	1.01×10^{-26}	6.33×10^{-27}	4.84×10^{-27}	3.61×10^{-27}	2.48×10^{-27}	1.60×10^{-27}
50 K	6.76×10^{-25}	2.78×10^{-25}	1.28×10^{-25}	7.64×10^{-26}	7.43×10^{-26}	4.81×10^{-26}	4.31×10^{-26}	2.70×10^{-26}	1.71×10^{-26}	1.13×10^{-26}	8.85×10^{-27}	6.68×10^{-27}	4.65×10^{-27}	3.01×10^{-27}
70 K	7.03×10^{-25}	3.04×10^{-25}	1.53×10^{-25}	9.98×10^{-26}	9.73×10^{-26}	6.88×10^{-26}	6.32×10^{-26}	4.32×10^{-26}	2.92×10^{-26}	2.01×10^{-26}	1.60×10^{-26}	1.22×10^{-26}	8.54×10^{-27}	5.55×10^{-27}
100 K	7.57×10^{-25}	3.57×10^{-25}	2.04×10^{-25}	1.46×10^{-25}	1.43×10^{-25}	1.09×10^{-25}	1.02×10^{-25}	7.46×10^{-26}	5.28×10^{-26}	3.72×10^{-26}	2.97×10^{-26}	2.26×10^{-26}	1.56×10^{-26}	9.87×10^{-27}

Table 5. Predicted emissivities in the IRAS, Herschel, and Planck photometric bands, deduced from the TLS model with the standard parameters given in Table 4, as a function of temperature. The emissivities have been normalized to 1×10^{-25} cm^2/H, at 250 μm for a temperature of 17.5 K. Note: Table 5 is also available in machine-readable form in the electronic edition of *A&A*.

Fit	λ bands	n	γ_0	γ_1	γ_2	γ_3	γ_4	γ_5
free T_d, β	[100-500] μm	4	-2.80348	1.38870	-0.0141556	5.37193×10^{-5}	-1.51050×10^{-7}	–
free T_d, β	[100-850] μm	5	-0.328268	1.17842	-0.0117752	5.28944e-05	-8.77938e-08	2.81994e-11
free T_d, β=2	[100-500] μm	4	13.7673	-1.99513	0.226583	-0.00715176	8.32780e-05	–
free T_d, β=2	[100-850] μm	5	-17.8000	8.38173	-1.05454	0.0673555	-0.00197337	2.18602e-05

Table 6. Polynomial coefficients (see Eq. 20) relating the dust temperature derived from the TLS model and those derived from a modified black-body fit.
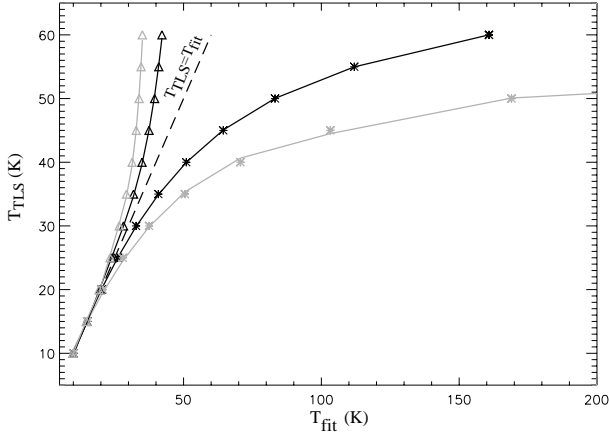
Fig. 9. Temperature derived using the TLS model (T_{TLS}) using the standard parameters given in Table 4, as a function of temperature derived from a modified black-body fit with a free β parameter (T_{fit}) in the IRAS 100 μm - Herschel 160, 250, 350, and 500 μm channels (black stars), and in the IRAS 100 μm - Planck 350, 550, and 850 μm channels (gray stars). The triangles show the temperatures derived from a modified black-body fit with β = 2, using the IRAS-Herschel channels (black) and the IRAS-Planck channels (gray). The dashed line corresponds to T_{fit} = T_{TLS}. The continuous lines shows the best polynomial fits.

Obviously, the exact profile of the emission spectrum depends on parameters that define the disorder, i.e. the amorphous structure of a material. Indeed, the amorphous state is not well defined as crystals, and atoms can be organized in a variety of local arrangements giving rise to a diversity of structures on short and medium length scales. But the emission profiles present some common characteristics: in the low-temperature range a spectral index value of the order of 2 in the FIR range, followed by variations in the β towards higher or lower values at longer wavelengths. As the temperature increases, the absorption is enhanced and is characterized by β values that decrease. These specificities can be observed in Figure 6, for the given sets of parameters that fit the observational data. However, this general behavior is also observed in laboratory experiments performed on amorphous materials and grains of astrophysical interest (Agladze et al., 1996; Mennella et al., 1998; Boudet et al., 2005). In particular, recent studies on three analogs of amorphous silicate Mg_2SiO_4, $MgSiO_3$, and $CaMgSi_2O_6$ reveal that this temperature and wavelength dependence of the absorption is observed on all the samples, but disappear when the same samples are annealed until crystallization (Coupeaud et al., 2011).These analyses indicate that the T_d-β variations are likely to result from intrinsic dust properties that can be reproduced for the first time by a dust emission model such as the TLS one.

7. Conclusions

The theoretical TLS model described in a previous work (Paper I) and based on the amorphous structure of grains was compared to astrophysical data, such as the FIRAS/WMAP and Archeops data. The FIRAS/WMAP spectrum represents the diffuse interstellar medium in the stellar neighborhood, whereas the Archeops data characterize dust properties in a variety of compact sources, where a significant inverse relationship between the dust temperature and the emissivity spectral index had been proven. We performed a χ^2 minimization to determine standard values for the parameters of the TLS model selected to capture the spectral and temperature variations in the model. These free parameters are the dust temperature (T_d), the charge correlation length (l_c) that controls the wavelength where the inflection point between the two β = 2 and β = 4 ranges occurs, the intensity factor of the TLS processes (A) with respect to the DCD effect, and the intensity factor of the TLS/hopping process (c_Δ). Results indicate that emission in the submm/mm is dominated by the hopping relaxation. According to the model, the BG emission in the FIR/mm domain depends on wavelength and temperature, which is fundamental both for dust mass determination from FIR/submm measurements but also for component separation.

Using the best-fit parameters (T_d = 17.26 K, l_c=13.4 nm, A=5.81, and c_Δ=475) allowing reproduction of both the emission from the diffuse medium and the compact sources, the model predicts significant β variations for temperatures between 5 and 100 K, with a maximum value of 2.6 at 2 mm. The TLS model is presently the only model able to predict β variations with temperature and wavelengths, as observed in both observational and laboratory data. The dust emissivity can be seriously underestimated if its variations with temperature and wavelength are not taken properly into account, generally inducing overestimates of the dust mass. Similarly, the comparison between temperatures derived from the TLS model (T_{TLS}) and those derived from a T_d-β fit (T_{fit}), between 100 and 500 μm, or 100 and 850 μm, are in good agreement for temperatures below 25 K. Above this value, the derived temperatures differ significantly from each other, in particular when emission far from the emission peak is considered in the fit. Indeed, a modified black-body fit is too simplistic to reproduce the mm emission excess, which increases with temperature. However, our study enables the possibility of deducing T_{TLS} from a given T_{fit}. We also predicted dust emissivities in the IRAS 100 μm, Herschel, and Planck bands for T_{TLS} between 5 and 100 K, which are useful for comparison with the Planck and Herschel data. For instance, the provided tables and figures can be used to derive the charge correlation length and the intensity of the TLS processes from the Herschel and Planck data.

The TLS model is the first physically-motivated model able to reproduce both diffuse medium and compact sources, observed with FIRAS/WMAP and Archeops. In the future, the Planck data will be used to systematically compare the model prediction with submm data.

References

Agladze, N. I., Sievers, A. J., Jones, S. A., et al. 1996, ApJ, 462, 1026

Anderson, P. W., Halperin, B. I., & Varma, C. M. 1972, Phil. Mag., 25, 1

Andriesse, C. D. 1974, A&A, 37, 257

Benoît, A., Ade, P., Amblard, A., et al. 2003, A&A, 399, 25

Bernard, J.-P., Abergel, A., Ristorcelli, I., et al. 1999, A&A, 347, 640

Bösch, M. 1978, Physical Review Letters, 40, 879

Bot, C., Boulanger, F., Rubio, M., & Rantakyro, F. 2007, A&A, 471, 103

Boudet, N., Mutschke, H., Nayral, C., et al. 2005, ApJ, 633, 272

Boulanger, F., Abergel, A., Bernard, J.-P., et al. 1996, A&A, 312, 256

Coupeaud, A., Demyk, K., Meny, C., et al. 2011, A&A, submitted

Dale, D. A., Helou, G., Contursi, A., et al. 2001, ApJ, 549, 215

Désert, F.-X., Macías-Pérez, J. F., Mayet, F., et al. 2008, A&A, 481, 411

Dickey, J. M., & Lockman, F. J. 1990, Ann. Rev. Astron. Astroph., 28, 215

Dickinson, C., Davies, R. D., & Davis, R. J. 2003, MNRAS, 341, 369

Draine, B. T., & Fraisse, A. A. 2009, ApJ, 696, 1

Dupac, X., Giard, M., Bernard J-P., et al. 2001, ApJ, 553, 604

Dupac, X., Giard, M., Bernard, J.-P., et al. 2002, A&A, 392, 691

Dupac, X., Boudet, N., Giard, M., et al. 2003, A&A, 404, L11

Finkbeiner, D. P., Davis M., Schlegel D.J. 1999, ApJ, 524, 867

Finkbeiner, D. P., Langston, G. I., & Minter, A. H. 2004, ApJ, 617, 350

Fitzgerald, S. A., Sievers, A. J., & Campbell, J. A. 2001a, J. Phys. Condens. Matter, 13, 2177

Fitzgerald, S. A., Campbell, J. A., & Sievers, A. J. 2001b, J. Phys. Condens. Matter, 13, 2095

Galliano, F., Madden, S. C., Jones, A. P., et al. 2005, A&A, 434, 867

Gromov, V., et al. 2011, in preparation

Hartmann, D., & Burton, W. B. 1995, Atlas of Galactic HI emission, Cambridge University Press

Hubbard, B. E., Tu, J. J., Agladze, N., & Sievers, A. J. 2003, Phys. Rev. B, 67, 144201

Jarosik, N., Bennett, C. L., Gold, B., et al. 2011, ApJS, 192, 14

Johnstone, D., & Bally, J. 1999, ApJ, 510, L49

Kemper, F., Vriend, W. J., & Tielens, A. G. G. M. 2004, ApJ 609,826

Malinen, J., Juvela, M., Collins, D. C., et al. 2011, A&A, 530, 101

Mennella, V., Brucato, J. R., Colangeli, L., et al. 1998, ApJ, 496, 1058

Mény, C., Gromov, V., Boudet, N., et al. 2007, A&A, 468, 171 (Paper I)

Miville-Deschênes, M.-A., & Lagache, G. 2005, ApJS, 157, 302

Paradis, D., Bernard, J.-P, & Mény, C. 2009, A&A, 506, 745

Paradis, D., Veneziani, M., Noriega-Crespo, A., et al. 2010, A&A, 520, L8

Paradis, D. et al. 2011, in preparation

Phillips, W. 1972, J. Low Temp. Phys., 11, 757

Phillips, W. 1987, Rep. Prog. Phys., 50, 1657

Planck collaboration 2011a, Planck early results 17, submitted to A&A, arXiv1101.2046

Planck collaboration 2011b, Planck early results 19, submitted to A&A, arXiv1101.2029

Planck collaboration 2011c, Planck early results 20, submitted to A&A, arXiv1101.2031

Planck collaboration 2011d, Planck early results 21, submitted to A&A, arXiv1101.2032

Planck collaboration 2011e, Planck early results 23, submitted to A&A, arXiv1101.2035

Planck collaboration 2011f, Planck early results 24, submitted to A&A, arXiv1101.2036

Planck collaboration 2011g, submitted to A&A, arXiv1101.2037

Reach, W.T., Dwek, E., Fixsen, D.J., & Hewagama, T. et al., 1995, ApJ, 451, 188

Schlegel, D. J., Finkbeiner, D. P., & Davis, M. 1998, ApJ, 500, 525

Schlömann, E. 1964, Phys. Rev., 135, 413

Shetty, R., Kauffmann, J., Schnee, S., et al. 2009, ApJ, 696, 2234

Stepnik, B., Abergel, A., Bernard, J.-Ph., et al. 2003, A&A, 398, 551

Veneziani, M., Ade, P. A. R., Bock, J. J., et al. ApJ, 2010, 713, 959

Vinogradov, V. S. 1960, Fiz. Tverd. Tela, 2, 2622 (English transl 1961, Sov. Phys. -Solid St. 2, 2338)